Transformation-Optics Description of Plasmonic Nanostructures Containing Blunt Edges/Corners: From Symmetric to Asymmetric Edge Rounding
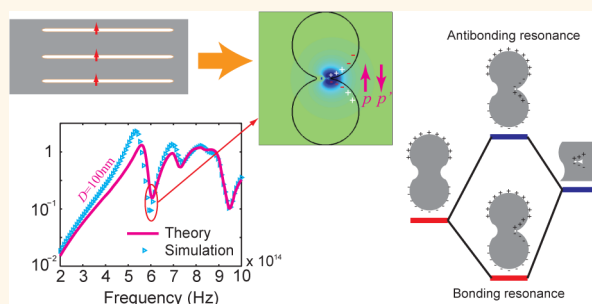
Yu Luo,[*,†] **Dang Yuan Lei,**[†] **Stefan A. Maier, and John B. Pendry**

The Blackett Laboratory, Department of Physics, Imperial College London, London SW7 2AZ, U.K. [†]These authors contribute equally.

The ability of harvesting light and efficiently concentrating its energy into a deep subwavelength volume is highly desired for many applications, such as fluorescence and photoluminescence,[1,2] super-resolution imaging,[3,4] Raman scattering spectroscopy,[5] single-molecule detection,[6,7] and nonlinear effect on the nanoscale.[8−10] Surface plasmons (SPs)[11−16] have made these applications possible through a strong interaction between the incident light and free electrons in metals. Critical to these goals is an ability to fully characterize and model the plasmonic properties of metallic nanostructures. With a tight control over the nanostructures in terms of size and shape, light can be effectively localized down to the nanometer-length scale and manipulated with unprecedented accuracy.[17−34] From traditional concepts, it is usually believed that a metallic structure should have a large physical size (as compared to the wavelength) to allow for a broadband light-harvesting process and a nanoparticle of finite size usually sustains SP resonances at discrete, rather than continuous frequencies. However, there are exceptions to these rules. Recent theoretical studies based on transformation optics[35,36] have shown that a finite nanostructure with sharp edges/corners behaves like an infinite plasmonic system. Such sharp geometrical features act as singularities for SPs, causing them to propagate toward the sharp points, slowing down as they progress. Consequently, the resonance spectrum becomes continuous as light energy builds up around the singularities.[37−42]

In practice, however, such perfectly sharp geometrical boundaries are unlikely to be realized. Hence, the control of the optical responses of more general blunt plasmonic structures requires a rigorous theory able to

understand the underlying physical mechanisms. In a recent study, we have proposed an analytical approach to study plasmonic nanostructures containing blunt tips.[43] A direct consequence of the edge rounding is the quantization of all the SP modes, which will blue-shift toward the surface plasmon frequency when the edge/corner

ABSTRACT

The sharpness of corners/edges can have a large effect on the optical responses of metallic nanostructures. Here we deploy the theory of transformation optics to analytically investigate a variety of blunt plasmonic structures, including overlapping nanowire dimers and crescent-shaped nanocylinders. These systems are shown to support several discrete optical modes, whose energy and line width can be controlled by tuning the nanoparticle geometry. In particular, the necessary conditions are highlighted respectively for the broadband light absorption effect and the invisibility dips that appear in the radiative spectrum. More detailed discussions are provided especially with respect to the structures with asymmetric edge rounding. These structures can support additional subradiant modes, whose interference with the neighboring dipolar modes results in a rapid change of the scattering cross-section, similar to the phenomenon observed in plasmonic Fano resonances. Finite element numerical calculations are also performed to validate the analytical predictions. The physical insights into blunt nanostructures presented in this work may be of great interest for the design of broadband light-harvesting devices, invisible and noninvasive biosensors, and slowing-light devices.

KEYWORDS: plasmonics · blunt nanostructures · transformation optics · broadband light harvesting · Fano resonance
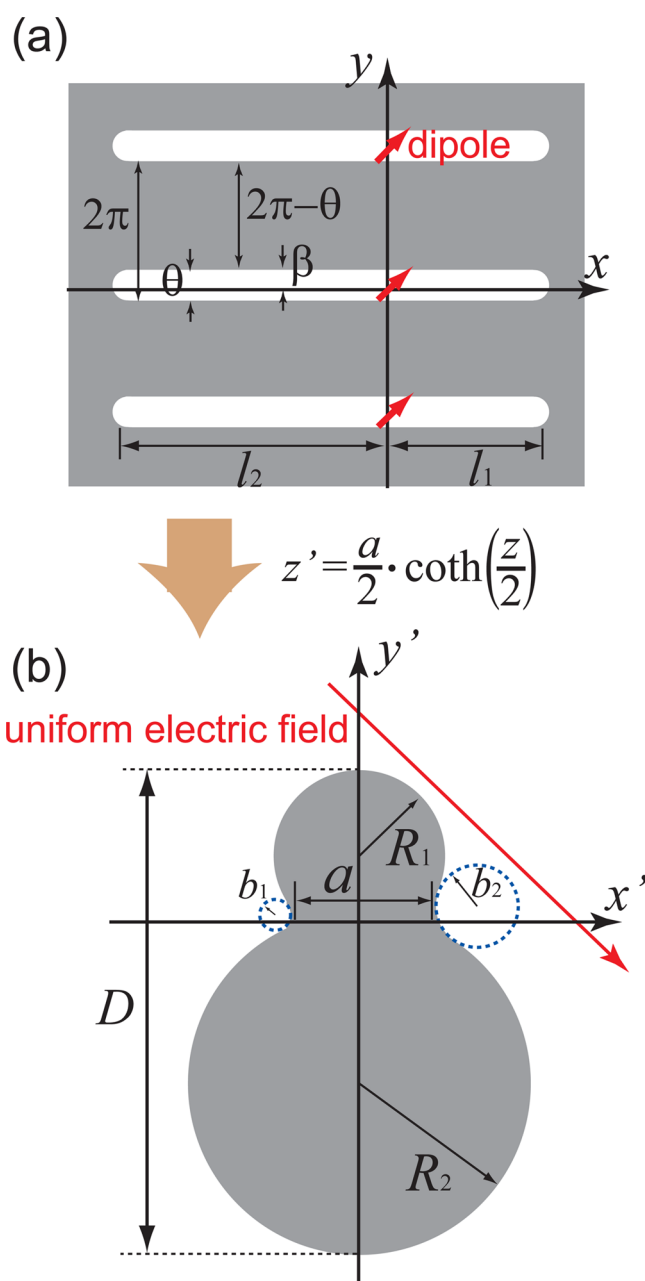
Figure 1. (a) 2D periodic plasmonic cavities support surface plasmon resonances that can be excited by an array of line dipoles (red arrows). The line dipole array is aligned along the y-axis, with a pitch of 2π. (b) The transformed geometry consists of two overlapping nanowires with blunt corners at the touching point. The source of the line dipole array is mapped into a uniform electric field.

bluntness increases. Nonetheless, a properly designed nanoparticle, such as the two-dimensional (2D) nanocrescent, is still found to exhibit a relatively broadband absorption cross-section which is nearly insensitive to the tip bluntness. This broadband behavior can be explained by the overlap of all the resonance bands due to the hybridization of SPs at the crescent tips. In fact, the general strategy reported in ref 43 is not restricted to the crescent structure. By applying appropriate conformal mappings to different canonical plasmonic systems, we can investigate a large number of complex nanostructures with blunt edges/corners, and

hence inversely design their optical properties according to the requirement of practical applications.

In this article, the general transformation strategy is applied to a broad variety of plasmonic systems. We start with a pair of overlapping nanowires with blunt corners, as shown in Figure 1b. General analytical formulas for the absorption and scattering cross sections as well as the local electric field enhancements are obtained within and beyond the quasi-static limit. Considering a bluntness diameter of 0.5 nm as the limit for neglecting the quantum mechanic effect,[44,45] the nanowire dimer can induce a maximum field

enhancement larger than 100. Our theoretical results also suggest that the extinction properties of the structure are directly related to the distance between the two geometrical corners (i.e., the parameter a shown in Figure 1b). A nanowire dimer with a larger distance between the two corners is more robust to edge rounding, but supports less SP modes, and vice versa. In addition, we find that the superposition of two neighboring bright modes results in an enhancement of absorption in the near-field, and a suppression of scattering in the far-field. Consequently, a so-called invisibility dip[46,47] appears in the radiative spectrum, where the absorption cross-section is about 1 order of magnitude larger than the scattering cross-section.

In the second part of this paper, we extend our study to asymmetrically blunt plasmonic nanostructures (i.e., the nanowire dimer containing two asymmetric corners and the 2D crescent with asymmetrically blunt claws). The theoretical calculation based on transformation optics shows that these structures can support a dark mode resonance characterized by a very sharp dip in the extinction spectrum. At this dip, energy is trapped at the sharper corner of the structure, similar to what happens in the plasmonic analogue of Fano resonance.[48−55] However, different from the plasmonic Fano resonance, the excitation of the dark mode does not result from the coupling to an adjacent bright mode, but is due to the interference between the SP resonances supported by the structure. To further understand the physical mechanism behind this phenomenon, the crescent-shaped nanostructures are investigated in detail. We find that, to observe this Fano-like interference, the structure must be mirror-symmetric in one direction, while strongly asymmetric in the perpendicular direction. Numerical simulations are performed to validate our analytical studies, and remarkable agreements are found for a structure dimension of up to 100 nm.

Transformation of the Geometry. In this section, the general transformation strategy is exposed, which will form the basis of the following discussion. This strategy can be explained through the example shown in Figure 1. A pair of overlapping nanowires containing two blunt corners (Figure 1b) can be related to an array of 2D metallic cavities (Figure 1a) through the following transformation:

$$z' = \frac{a}{2}\coth\left(\frac{z}{2}\right) \tag{1}$$

where $z = x + iy$ and $z' = x' + iy'$ are the usual complex number notation in the original and transformed frames, respectively; the parameter a stands for the distance between the two corners of the nanowire dimer, which we will refer to as the overlapping distance in the following part of this paper. The other geometrical parameters in Figure 1b, such as the

nanowire radii R_1 and R_2, and the total structure dimension D can be expressed as

$$R_1 = \frac{a}{2\sin(\theta - \beta)} \tag{2}$$

$$R_2 = \frac{a}{2\sin\beta} \tag{3}$$

$$D = \frac{a}{2}\left[\cot\frac{\theta}{2} + \cot\left(\frac{\theta - \beta}{2}\right)\right] \tag{4}$$

Note that the transformation associated with periodic infinitely long metallic slabs has been widely discussed in refs 41, 56, and 57. In those cases, infinity in the original coordinate frame is mapped to the perfectly sharp geometrical boundaries that act as energy sinks for the SP modes. As a result, the transformed nanostructures can induce extremely large field enhancements and exhibit a continuous absorption spectrum over a broad frequency band. In this case, however, the perfectly sharp corners at the overlapping parts of the nanowires are turned blunt (see Figure 1b). Accordingly in the original coordinate frame, the thin dielectric films between the metal slabs are truncated on both sides, as shown in Figure 1a. In other words, the nanowire dimer is equivalent to an array of finite plasmonic cavities. The distance between the origin and the truncated points determines the bluntness radii b_1 and b_2 of the two corners:

$$b_{1(2)} = (4De^{l_{1(2)}}\sin\beta)$$

$$\Big/ \left((e^{l_{1(2)}} - 1)[e^{l_{1(2)}}(1 - \sin\beta) - (1 + \sin\beta)]\left(\cot\frac{\beta}{2} + \cot\frac{\theta - \beta}{2}\right) \right) \tag{5}$$

The above equation indicates that the farther we truncate the dielectrics, the sharper the two corners are.

The transformation of electromagnetic sources is also illustrated in Figure 1. In the initial space (i.e., $x−y$ frame), the source is an array of line dipoles, each element of which has a dipole moment $\bar{p} = \hat{x}p_x + \hat{y}p_y$ (where $\hat{x}$ and $\hat{y}$ are the unit vectors corresponding to the x and y directions). Under the conformal mapping, the line dipole array is transformed into a uniform electric field:

$$\bar{E}_0' = \frac{1}{2\pi\varepsilon_0 a}(\hat{x}p_x - \hat{y}p_y) \tag{6}$$

When the total dimension of the nanowire pair is much smaller than the incoming wavelength λ, the uniform electric field can be considered as an incident plane wave, and the SP modes are well described in the quasi-static approximation. In this case, the magnetic and electric fields are decoupled, and the latter can be related to an electrostatic potential that fulfills Laplace's equation.[58] Under the 2D conformal mapping,
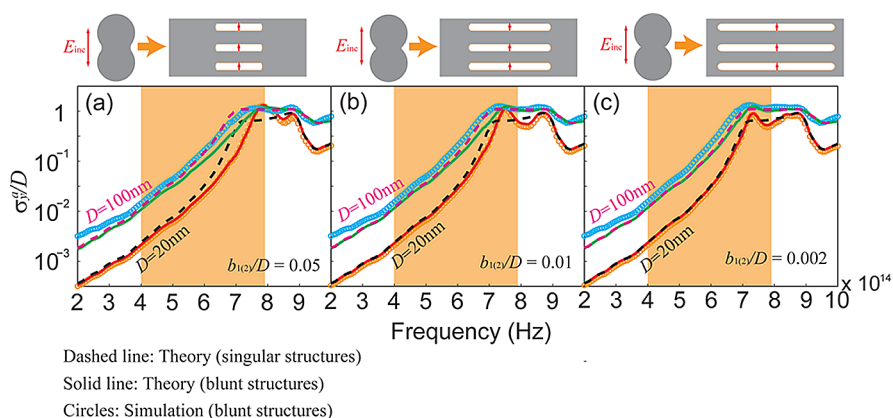
Figure 2. Absorption cross sections σ_y^a normalized by the overall physical cross-section D for overlapping nanowire dimers with different bluntness dimensions: (a) $b_1 = b_2 = 0.05D$; (b) $b_1 = b_2 = 0.01D$; (c) $b_1 = b_2 = 0.002D$. In each case, structures of two different sizes ($D = 20$ nm and $D = 100$ nm) are considered, while the overlapping distance is fixed as $a = R$. The shaded (orange) regions in the subfigures indentify the visible spectrum. The inset of each figure shows the schematic of the geometry considered and the corresponding plasmonic cavity before transformation. Theoretical calculations are compared with numerical simulations.

the dielectric properties of the nanostructure remain unchanged for P-polarized wave, and the electrostatic potential is preserved:

$$\phi(x, y) = \phi'(x, 'y') \tag{7}$$

The electric field in the transformed $x' - y'$ coordinate frame can then be obtained:

$$\bar{E}' = -\hat{x}\frac{\partial \phi'}{\partial x'} - \hat{y}\frac{\partial \phi'}{\partial y'} \tag{8}$$

Thus, the blunt overlapping nanowires shown in Figure 1b can be studied analytically by solving the problem of periodic plasmonic cavities shown in Figure 1a.

Quasi-static Solution. This section summarizes the solution to the nanowire dimer problem in the quasi-static limit. Detailed derivations are provided in the Methods section. In the first step, we rewrite the electrostatic potential associated with the line dipole source through a Fourier transform, and study the SP modes supported by the periodic plasmonic cavities in the k-space. Then, by applying an inverse Fourier transform to the k-space solution, the induced potential in the real space can be obtained (eqs 30 and 35), which in turn gives the electric fields in the slab geometry (eqs 40−43). Finally, the extinction cross-section σ_e and scattering cross-section σ_s of the nanowire dimer can be deduced from the backscattered field at the dipole position:

$$\sigma_e^x = -\frac{4k_0a^2}{(\tau_1 + \tau_2)^2}\text{Im}\{\xi_{xx}\},$$
$$\sigma_e^y = -\frac{4k_0a^2}{(\tau_1 + \tau_2)^2}\text{Im}\{\xi_{yy}\} \tag{9}$$

$$\sigma_s^x = \frac{2k_0^3a^4}{(\tau_1 + \tau_2)^4}(|\xi_{xx}|^2 + |\xi_{xy}|^2),$$

$$\sigma_s^y = \frac{2k_0^3a^4}{(\tau_1 + \tau_2)^4}(|\xi_{yy}|^2 + |\xi_{xy}|^2) \tag{10}$$

where $\tau_1 = l_1/\pi$, $\tau_2 = l_2/\pi$; $k_0 = \omega(\varepsilon_0\mu_0)^{1/2}$ is the wave vector in free space; the other three coefficients ξ_{xx}, ξ_{yy}, and ξ_{xy} are calculated as

$$\xi_{xx} = \sum_n \frac{n\pi}{2}\left(1 + \cos\frac{2n\pi\tau_1}{\tau_1 + \tau_2}\right)((e^\alpha(\gamma_3^{2n} - 1)(\gamma_1^{2n} + \gamma_2^{2n})$$
$$- 2e^{2\alpha}\gamma_3^{2n} + 2(e^{2\alpha} - 1)\gamma_1^n\gamma_2^n\gamma_3^n + 2)/(e^{2\alpha}(\gamma_1^n\gamma_2^n - \gamma_3^n)^2$$
$$- (\gamma_1^n\gamma_2^n\gamma_3^n - 1)^2)) \tag{11}$$

$$\xi_{yy} = \sum_n \frac{n\pi}{2}\left(1 - \cos\frac{2n\pi\tau_1}{\tau_1 + \tau_2}\right)((e^\alpha(\gamma_3^{2n} - 1)(\gamma_1^{2n} + \gamma_2^{2n})$$
$$+ 2e^{2\alpha}\gamma_3^{2n} - 2(e^{2\alpha} - 1)\gamma_1^n\gamma_2^n\gamma_3^n - 2)/(e^{2\alpha}(\gamma_1^n\gamma_2^n - \gamma_3^n)^2$$
$$- (\gamma_1^n\gamma_2^n\gamma_3^n - 1)^2)) \tag{12}$$

$$\xi_{xy} = \left(\frac{\varepsilon_m - 1}{\varepsilon_m + 1}\right)\sum_n \frac{n\pi}{2}\left(\sin\frac{2n\pi\tau_1}{\tau_1 + \tau_2}\right)$$
$$\times(((e^{2n\pi d_3/L} - 1)(\gamma_1^n + \gamma_2^n)(\gamma_1^n - \gamma_2^n))/(e^{2\alpha}(\gamma_1^n\gamma_2^n - \gamma_3^n)^2$$
$$- (\gamma_1^n\gamma_2^n\gamma_3^n - 1)^2)) \tag{13}$$

where ε_m is the permittivity of metal, $\alpha = \ln[(\varepsilon_m - 1)/(\varepsilon_m + 1)]$, $\gamma_1 = e^{\beta/(\tau_1+\tau_2)}$, $\gamma_2 = e^{(\theta-\beta)/(\tau_1+\tau_2)}$, $\gamma_3 = e^{(2\pi-\theta)/(\tau_1+\tau_2)}$. Note that the extinction cross-section (eq 9) is proportional to the square of the overlapping distance a, while the scattering cross-section (eq 10) scales as the fourth power of a. Under the quasi-static approximation, we have $k_0a \ll 1$, which indicates $\sigma_s^{x,y} \ll \sigma_e^{x,y}$. In this case, the absorption cross-section of the nanowire dimer is approximately equal to the extinction cross-section ($\sigma_a^{x,y} = \sigma_e^{x,y} - \sigma_s^{x,y} \approx \sigma_e^{x,y}$).

Equations 11−13 also show that the absorption/scattering cross-section is the sum of the contribution from the SP modes denoted by their angular moment n. Each mode may result in a resonance as long as the following condition is satisfied:

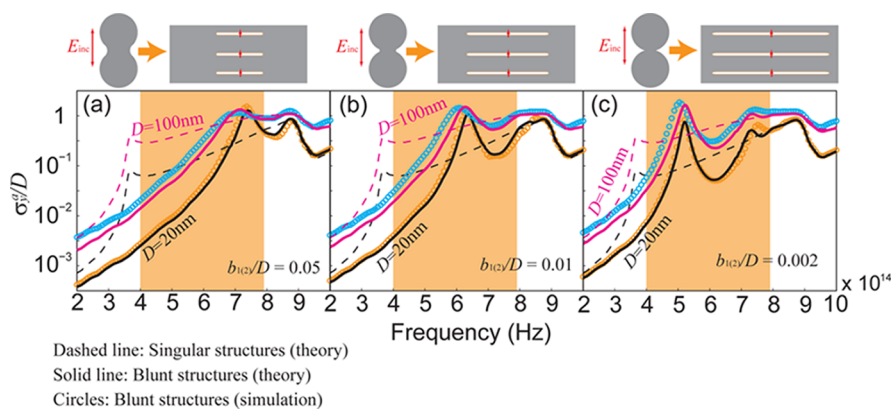$$e^{2\alpha}(\gamma_1^n\gamma_2^n - \gamma_3^n)^2 - (\gamma_1^n\gamma_2^n\gamma_3^n - 1)^2 = 0 \tag{14}$$

Figure 3. Absorption cross sections σ_y^a normalized by the overall physical cross-section D for overlapping nanowire dimers with different bluntness dimensions: (a) $b_1 = b_2 = 0.05D$; (b) $b_1 = b_2 = 0.01D$; (c) $b_1 = b_2 = 0.002D$. In each case, structures of two different sizes ($D = 20$ nm and $D = 100$ nm) are considered, while the overlapping distance is fixed as $a = 0.2R$. The shaded (orange) region in each subfigure indentifies the visible spectral range. The inset of each figure shows the schematic of the geometry considered and the corresponding plasmonic cavity before transformation. Theoretical calculations are compared with numerical simulations.
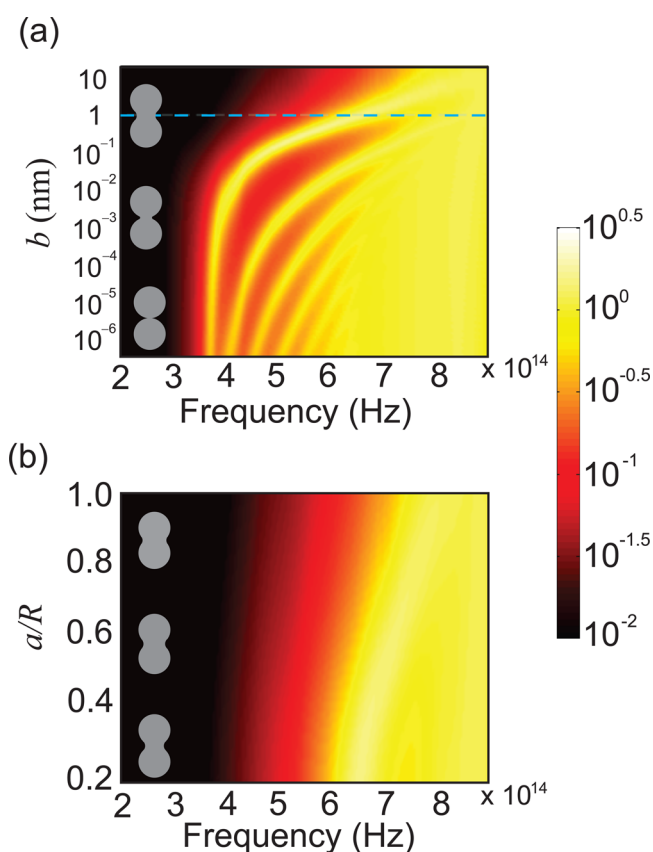

Figure 4. (a) Normalized absorption cross-section σ_y^a/D as a function of frequency and the bluntness dimension of the geometry corners. Here the overlapping distance is fixed as $a = 0.2R$, and the total structure dimension is set as $D = 100$ nm. The blue dashed line indentifies the optimal bluntness ($b = 1$ nm) where the overlap of all the SP resonances results in a relatively continuous absorption spectrum. (b) Normalized absorption cross sections σ_y^a/D as a function of the frequency and the normalized overlapping distance a/R. Here the bluntness of the geometry corners is fixed at $b = 1$ nm, and the total structure dimension is set as $D = 100$ nm.

Equation 14 implies that the resonance condition only depends on the geometry of the nanostructure.

Solution beyond the Quasi-static Limit. The quasi-static solution presented in the former section is only valid when the total dimension of the nanostructure is sufficiently small, typically $D \leq 20$ nm (considering the visible frequency range). To extend our study beyond this limit, we have to take into account the radiative damping in the dimer geometry. Since dipoles and fields exchange roles under the transformation

denoted by eq 1, the radiative damping in the transformed coordinate frame can be modeled as a fictional absorbing dipole in the original slab frame.[59] Detailed calculations (provided in the Methods section) show that the modified extinction and scattering cross sections take the following form:

$$\sigma_e^x = -\frac{4k_0a^2}{(\tau_1+\tau_2)^2}\,\mathrm{Im}\left\{\frac{\xi_{xx}+i\eta(\xi_{xx}\xi_{yy}+\xi_{xy}^2)}{(1+i\eta\xi_{xx})(1+i\eta\xi_{yy})-(\eta\xi_{xy})^2}\right\}$$

$$\sigma_e^y = -\frac{4k_0a^2}{(\tau_1+\tau_2)^2}\,\mathrm{Im}\left\{\frac{\xi_{yy}+i\eta(\xi_{xx}\xi_{yy}+\xi_{xy}^2)}{(1+i\eta\xi_{xx})(1+i\eta\xi_{yy})-(\eta\xi_{xy})^2}\right\}$$

$$(15)$$

$$\sigma_s^x = \frac{2k_0^3a^4}{(\tau_1+\tau_2)^4}\left(\left|\frac{\xi_{xx}+i\eta(\xi_{xx}\xi_{yy}+\xi_{xy}^2)}{(1+i\eta\xi_{xx})(1+i\eta\xi_{yy})-(\eta\xi_{xy})^2}\right|^2\right.$$
$$\left.+\left|\frac{\xi_{xy}}{(1+i\eta\xi_{xx})(1+i\eta\xi_{yy})-(\eta\xi_{xy})^2}\right|^2\right)$$

$$\sigma_s^y = \frac{2k_0^3a^4}{(\tau_1+\tau_2)^4}\left(\left|\frac{\xi_{yy}+i\eta(\xi_{xx}\xi_{yy}+\xi_{xy}^2)}{(1+i\eta\xi_{xx})(1+i\eta\xi_{yy})-(\eta\xi_{xy})^2}\right|^2\right.$$
$$\left.+\left|\frac{\xi_{xy}}{(1+i\eta\xi_{xx})(1+i\eta\xi_{yy})-(\eta\xi_{xy})^2}\right|^2\right) \quad (16)$$

Here the scaling factor η is calculated as

$$\eta = \frac{1}{2}\left(\frac{k_0a}{\tau_1+\tau_2}\right)^2 \quad (17)$$

All the other coefficients (i.e., $\tau_1, \tau_2, \xi_{xx}, \xi_{yy}, \xi_{xy}$) in eqs 15 and 16 have been defined in the former section. It is worth noticing that, when $a \ll \lambda$, the scaling factor $\eta \rightarrow 0$. Equations 15 and 16 are reduced to eqs 9 and 10, which are the quasi-static solutions. Finally, the absorption cross-section can be deduced:

$$\sigma_a^x = \sigma_e^x - \sigma_s^x,\ \sigma_a^y = \sigma_e^y - \sigma_s^y \quad (18)$$

RESULTS AND DISCUSSION

In this section, we validate our analytical theory outlined in the previous sections, by considering two examples, that is, a pair of overlapping nanowires (with blunt corners) and the crescent-shaped nanocylinder (containing blunt tips). For each structure, we examine how the geometry affects the energy and line width of each SP resonance, and compare the theoretical results with numerical simulations. In all the following discussions, the permittivity of the nanostructure ε_m is taken from experimental data for silver.[60]

Overlapping Nanowire Dimer with Symmetric Edge Rounding. We first consider the symmetric nanowire dimer; that is, the two wires composing the dimer have the same dimensions ($R_1 = R_2 = R$), and the bluntness radii at the two corners are equal $b_1 = b_2 = b$.

Figure 2 shows the absorption cross sections for three nanowire dimers with the same overlapping distance ($a = R$) but different bluntness radii. In each case, structures of two different dimensions are considered ($D = 20$ nm and $D = 100$ nm). Theoretical calculations are compared with numerical simulations, showing a nice agreement. By comparing the three subfigures, we find that this structure can only support a narrow absorption band, which is, however, robust to edge rounding (i.e., changing the bluntness radius b does not have much effects on the absorption spectrum).

We next consider a symmetric nanowire dimer with relatively small overlapping distance $a = 0.2R$. As displayed in Figure 3, all the SP modes redshift when the bluntness radius decreases, coinciding with the experimental observation for closely encountered nanoshells.[28] Therefore, compared to the results in Figure 2, the structure with smaller overlapping distance is more sensitive to the edge rounding. This phenomenon can be explained by the schematic of the geometry transformation. A large overlapping distance of the two nanowires corresponds to a large separation (weak hybridization) between the metallic slabs (see the insets above Figure 2). Hence, the SP modes supported by each slab are only slightly modified (red-shifted) due to the weak hybridization, and are all restricted in a frequency range close to the surface plasmon frequency. Since all the resonance bands overlap with each other, the truncation distance of the dielectric slab (corresponding to the edge rounding) can only have limited effects on the bandwidth. On the contrary, a smaller overlapping distance (such as the one shown in Figure 3) allows for large deviation of the SP modes from surface plasmon frequency, which is more likely to be affected by the edge rounding.

To further determine how the geometry of the nanostructure affects the SP resonances, we calculate the normalized absorption cross-section σ_y^a/D for various bluntness dimension b and overlapping distance a. Figure 4a represents the dependence of σ_y^a/D on the frequency and the bluntness radius of geometrical corners, which demonstrates prominent redshifts of the SP modes as b decreases. Here, the overlapping distance is set as $a = 0.2R$, the same as in Figure 3. The blue dashed line highlights that when the bluntness radius is 1 nm, the overlap of all the SP resonances results in a relatively continuous absorption spectrum. On the other hand, in Figure 4b, both the total structure dimension and the bluntness radius are fixed ($D = 100$ nm, $b = 1$ nm), while σ_y^a/D is plotted as a function of the overlapping distance and the frequency. We can clearly find that decreasing the overlapping distance results in an increase of the bandwidth, while the spectrum still remains continuous. To conclude, to achieve broadband light harvesting with blunt touching
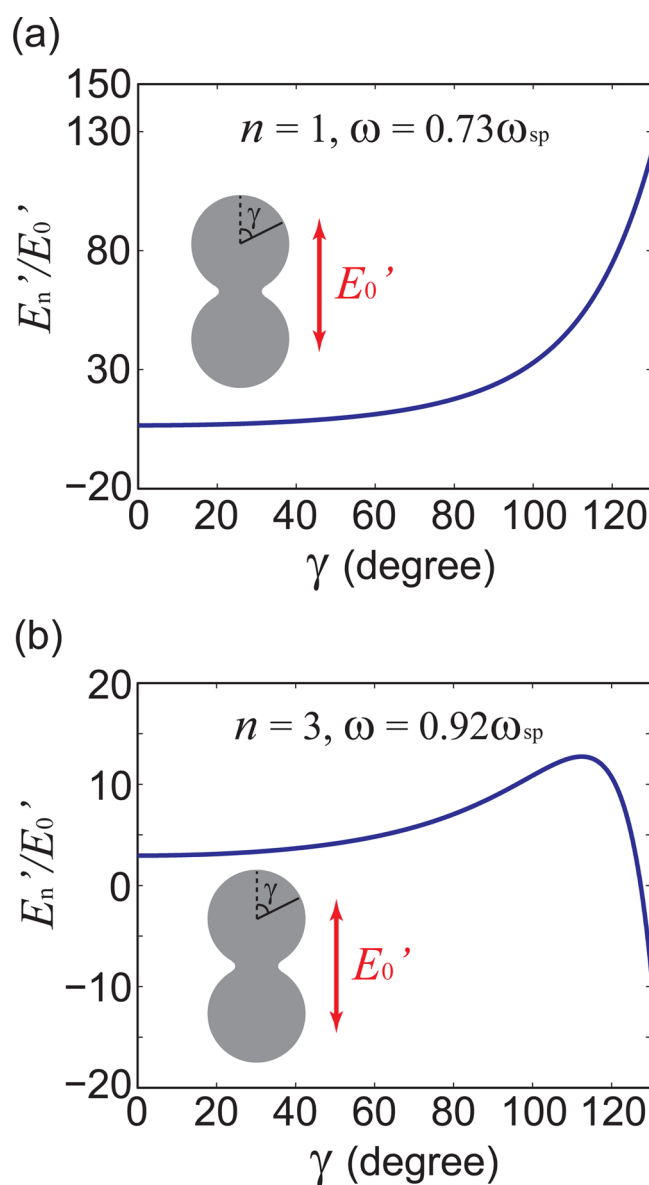
(a)

$n = 1$, $\omega = 0.73\omega_{sp}$

(b)

$n = 3$, $\omega = 0.92\omega_{sp}$

Figure 5. The imaginary part of E_n' normalized by the incident electric field E_0' along the nanowire surface at different frequencies; (a) $\omega = 0.73\omega_{sp}$ (the resonant frequency associated with the mode $n = 1$); (b) $\omega = 0.92\omega_{sp}$ (the resonant frequency associated with the mode $n = 3$). The geometrical parameters of the nanowire dimer are set as $a = 0.2R$, $b_1 = b_2 = 0.01D$. The angle γ is defined in the inset of each figure.

nanowires, one has to keep the distance between the two touching points as small as possible.

Now, we turn our attention to the electric fields induced in the near-field of the nanowire dimer. Figure 5 displays the analytical calculations at the first two resonances with the corresponding angular momentum $n = 1$ and $n = 3$ (from left to right). We can see that each resonance is related to a particular distribution of the electric field, with the maximum field enhancement induced around the corners of the overlapping part. Note that, different from the kissing nanowires in which the group velocity of SPs vanishes and energy accumulates at the touching point,[40,61] light cannot be stopped at the blunt corner of the overlapping nanowires. Instead, the SPs will be

reflected back after reaching this point, leading to the resonant behavior of the whole system. Nevertheless, very large field enhancements can still be achieved at the resonant frequencies, for example, the maximum field enhancement at the first resonance ($\omega = 0.73\omega_{sp}$) reaches up to 120 at the touching point.

At the end of this part, we study the scattering properties of the nanowire dimer. We focus our discussion on the structure of 100 nm dimension shown in Figure 3b. In this case, the bluntness radius is 1 nm, which is already realistic in practice. Figure 6 panels a and b compare the absorption (σ_y^a/D) and scattering (σ_y^s/D) cross sections for this structure. We can clearly see a sharp dip at $\omega = 676$THz in the scattering spectrum, where σ_y^s/D is about 1 order of magnitude smaller
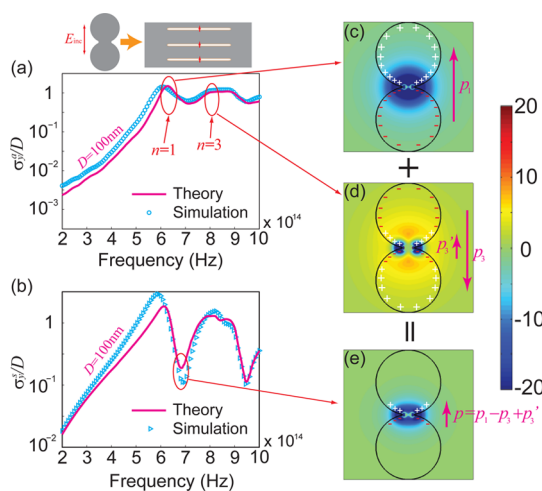
Figure 6. Normalized absorption cross-section σ_y^a/D (a) and scattering cross-section σ_y^s/D (b) as a function of frequency for an overlapping nanowire dimer with symmetrically blunt corners ($b_1 = b_2 = 0.01D$). Here the overlapping distance is set as $a = 0.2R$. Panels c, d, and e display the electric field distributions associated with the dipolar mode ($n = 1$), the higher order bright mode ($n = 3$), and the sharp dip between these two modes in the scattering spectrum, respectively.
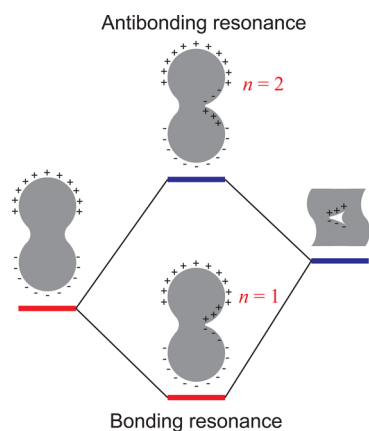

Figure 7. Illustration of the plasmonic hybridization arising from the interaction between two nanoparticles. The dipolar resonance of symmetrically blunt overlapping nanowires interacts with that of a triangular hole, giving rise to the bonding (superradiant) and antibonding (subradiant) modes supported by the asymmetrically blunt nanowire dimer.

than σ_y^a/D. As explained in ref 46, this sharp dip results from the interference between two neighboring bright modes, $n = 1$ and $n = 3$. Note that for a symmetric nanowire dimer, the SP modes with even angular moment (such as $n = 2$) are totally dark, and therefore cannot be excited in the far-field. Figure 6 panels c, d, and e display the electric field and surface charge distributions at the three frequencies corresponding to the two bright mode resonances ($n = 1$ and $n = 3$), and the scattering dip, respectively. The results indicate that at the scattering dip, the two bright modes interact constructively in the near-field, leading to a large field enhancement at the overlapping part even if
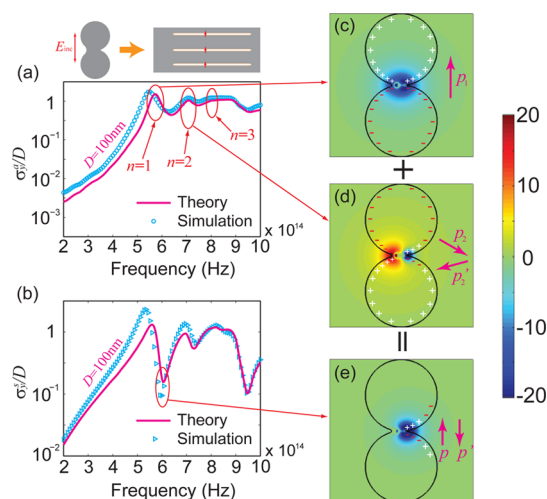
Figure 8. Normalized absorption cross-section σ_y^a/D (a) and scattering cross-section σ_y^s/D (b) as a function of frequency for an overlapping nanowire dimer with asymmetrically blunt corners ($b_1 = 0.01D$ and $b_2 = 0.002D$). Here the overlapping distance is set as $a = 0.2R$. Panels (c), (d), and (e) display the electric field distributions associated with the superradiant mode ($n = 1$), subradiant mode ($n = 2$), and Fano-like dip (which corresponds to the superposition of modes $n = 1$ and $n = 2$) in the scattering spectrum, respectively.

the SP modes are out of resonance. On the other hand, the interference between the bright modes is destructive in the far-field, giving rise to a weak radiative coupling (the total dipole moment of the structure is relatively small). In other words, at the scattering dip, the overlapping nanowire dimer can efficiently confine SPs at the nanoscale while scattering little light. This property may lead to the practical implementation of invisible or noninvasive biosensors, as has already been pointed out in the previous study.[46]

Overlapping Nanowire Dimer with Asymmetric Edge Rounding. In this part, we address the question on how the asymmetric edge rounding affects the optical responses of the nanostructure. The plasmonic hybridization model proposed by Peter Nordlander and colleagues[62−65] can be used to understand the complex plasmonic modes of the symmetry-broken nanowire pair. Figure 7 explains how the plasmon modes supported by the asymmetric nanowire dimer can be understood as the combination of bonding and antibonding plasmon modes in a symmetric nanowire dimer and a metal slice. Here we highlight that the antibonding mode has an even angular moment $n = 2$.

To quantitatively examine the optical response of the nanowire dimer with asymmetric edge rounding, we use the transformation method to calculate the spectrum of the SP modes. From Figure 8a, we find that due to the breaking of symmetry, these structures can support a superradiant mode (corresponding to the bonding mode resonance) at a low frequency and a subradiant mode (corresponding to the antibonding mode resonance) at a relatively high frequency, which agrees with the hybridization model. More interestingly, between these two
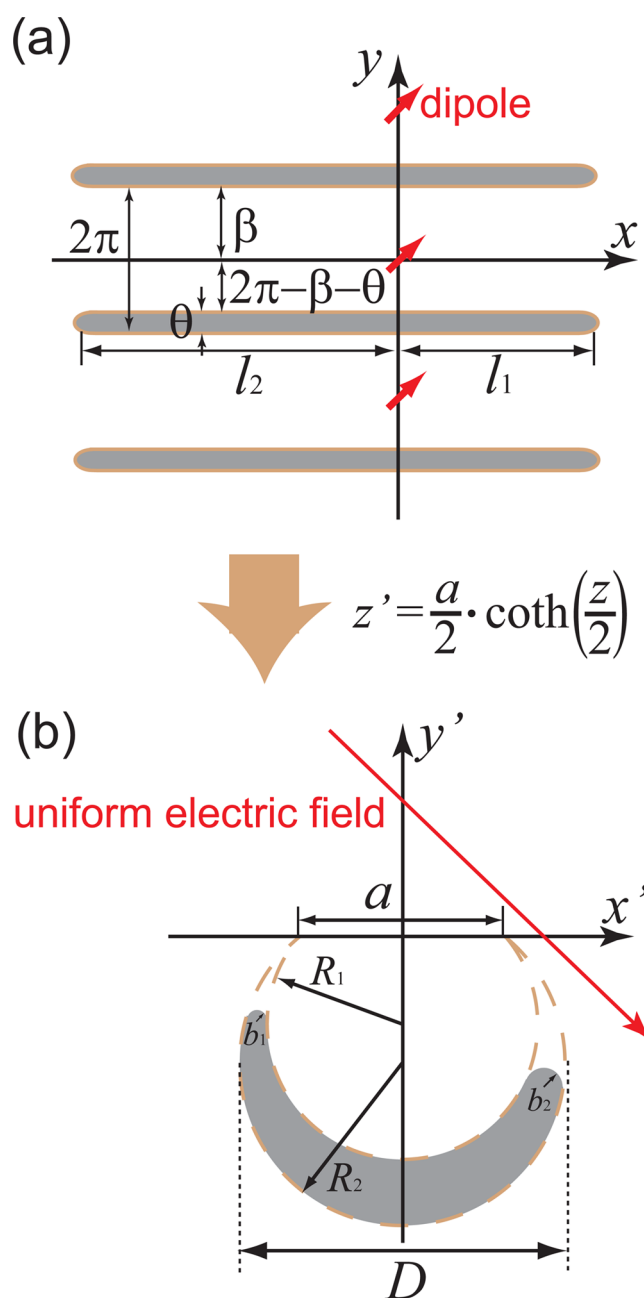
Figure 9. (a) Truncated periodic metallic slabs excited by a array of line dipoles. (b) 2D nanocrescent containing two blunt tips illuminated by a uniform electric field. These two configurations can be related to each other through a conformal mapping $z' = a/2 \coth(z/2)$.

resonant frequencies, the interference between the two modes leads to a dark mode resonance characterized by a sharp and asymmetric line shape in the scattering spectrum, as shown in Figure 8b. Figure 8 panels c and d depict the electric field distributions at the resonant frequencies of the modes $n = 1$ and $n = 2$, respectively. The cancellation of the dipole moments associated with the superradiant and subradiant modes results in a weak radiative coupling at the scattering dip (see the red arrows in Figure 8c−e). Different from the symmetric nanowire dimer discussed in the former section, here the asymmetrically blunt structure exhibits a nonzero quadrupole

moment at the sharp scattering dip. Figure 8e displays the electric field and surface charge distributions at the scattering dip, showing that the energy is trapped at the sharper corner of the structure, similar to the phenomenon of a plasmonic Fano resonance,[54] observed in a single metallic disk with a missing wedge-shaped slice. However, we stress that our case is not a Fano resonance, because the dark mode excitation does not result from the coupling between bright and dark modes.

2D Nanocrescent with Asymmetric Edge Rounding. To further understand the effect of asymmetric edge rounding and reveal the physical mechanism behind

the Fano-like interference, we consider a nanostructure with an even less symmetric shape, that is, 2D nanocrescents with asymmetric tip bluntness. As illustrated in ref 43, a 2D blunt nanocrescent can be studied by mapping it into an array of truncated metallic slabs (see Figure 9). Under the transformation, the geometrical parameters are calculated by

$$R_1 = \frac{a}{2\sin(\beta + \theta)} \quad (19)$$

$$R_2 = \frac{a}{2\sin\beta} \quad (20)$$

$$b_{1(2)} = \frac{R_2 \sin\beta \tan(\theta/2)}{|\sinh[(l_{1(2)} + i\beta)/2]||\sinh[(l_{1(2)} + i\beta + i\theta)/2]|} \quad (21)$$
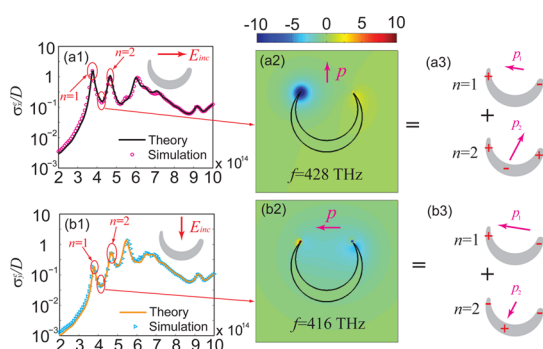

Figure 10. (a1−a3) Asymmetrically blunt crescent under an incident excitation with electric field polarized along the horizontal direction; (b1−b3) same structure as panels a but excited by a vertically polarized electric field. (a1, b1) Normalized extinction cross sections σ_y^e/D; (a2, b2) electric field distributions associated with the extinction dip; (a3, b3) illustration of the superposition of the modes $n = 1$ and $n = 2$. The geometrical parameters of the crescent are set as: $a = 70.7$ nm, $R_1 = 43.7$ nm, $R_2 = 50$ nm, $b_1 = 0.005D$, and $b_2 = 0.0005D$.

where R_1 and R_2 correspond to the inner and outer radius of the crescent, respectively; b_1 and b_2 stand for the bluntness radius at each tip. All the other parameters are depicted in Figure 9. To study the scattering/absorption property of this structure, we derive the extinction cross sections under incident fields of two orthogonal polarizations (Detailed derivations can be found in the Method section), as shown in Figure 10a1,b1. Figure 10 a2 and b2 correspond to the field distribution at the extinction dip in each polarization case. We notice that this structure can also support a subradiant mode (with an even angular moment $n = 2$) due to the breaking of symmetry. However, in contrast to the case of the overlapping nanowire dimer, the dipole moments of the first two bright modes supported by the 2D nanocrescent are not antiparallel, as depicted by Figure 10 panels a3 and b3. Therefore, the dip of the extinction spectrum does not correspond to a dark mode since the total dipole moment in this case is not equal to zero (see the red arrows in panels a2 and b2).

Increasing the degree of symmetry of the structure in the vertical direction finally makes the crescent a flat pike-like shape (with $R_1 = R_2$) which is mirror-symmetric, like the overlapping nanowires. In this case, the dipole moments associated with the modes $n = 1$ and $n = 2$ become antiparallel and cancel out each other at the scattering dip (see Figure 11d). Consequently, the dark mode resonance appears, where light energy is efficiently confined at the sharper tip of the nanostructure, as illustrated by Figure 11c. This indicates that the necessary condition to observe the Fano-like interference is for the structure to be asymmetric in one direction, while mirror-symmetric in the perpendicular direction.
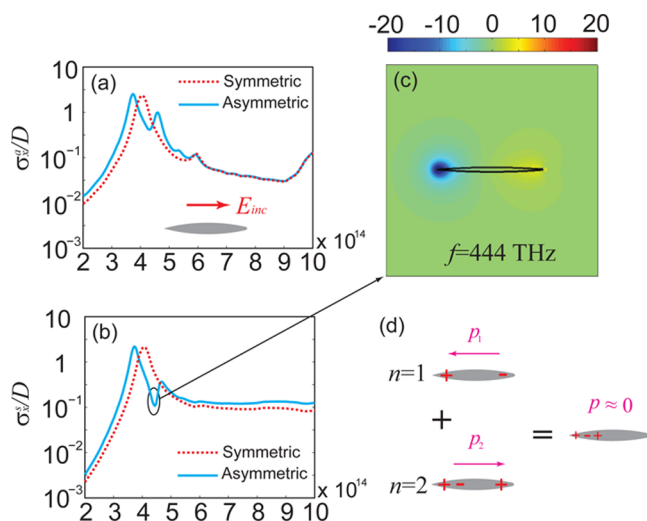

Figure 11. Symmetric and asymmetric pike-like nanostructures under an incident excitation with the electric field parallel to the lone axis: (a) the normalized absorption cross-section; (b) the normalized scattering cross-section; (c) the electric field distribution associated with the scattering dip; (d) illustration of the superposition of modes $n = 1, 2$. The geometrical parameters of the pike-like nanostructure are set as $a = 100$ nm, $R_1 = R_2 = 637.3$ nm, $b_1 = 0.005a$, and $b_2 = 0.0005a$.

CONCLUSION

This article presents a general analytical strategy to investigate plasmonic structure containing blunt edges/corners. We have analyzed how the edge rounding of the nanostructures can be engineered to achieve peculiar optical response including broadband or selective spectral dependence of absorbed and scattered light as well as large local electric field enhancements. These theoretical studies provide insightful understanding of the effect of geometrical parameters on the plasmonic properties. The ability to engineer the physical parameters of metallic nanostructures and thus to maneuver their optical responses provides great promise for the development of new devices and applications. Furthermore, theoretical models can predict unique plasmonic responses of novel structures that are yet to be fabricated, motivating further synthetic work in these areas. Finally, it should be pointed out that the retardation and quantum mechanical effects are not considered in our analytical calculations. Therefore, our transformation strategy is accurate when the bluntness size is larger than 0.5 nm and the total structure dimension is within the range from 10 nm to 200 nm. Out of these size ranges, a more general quantum description[44,45,66,67] and nonlocal constitutive relation[68,69] of metal may be necessary to further improve our analytical model.

METHODS

Overlapping Nanowires. The problem of periodic plasmonic cavities is depicted in Figure 1a. We first tackle this problem in the near field approximation, assuming Laplace's equation is obeyed. Strictly speaking, the SP modes supported by the periodic structure consist of the transverse modes (that propagate along the x direction) and the longitudinal modes (that propagate along the y direction). Since we are only interested in the case when $l_1 + l_2 \gg \theta$, we can neglect the contribution from the longitudinal modes, and assume that the SP excitations are mainly due to the transverse modes. As a result, the electrostatic potential in one period can be written as:

$$\frac{1}{1 - e^{2ik(l_1 + l_2)}}(e^{ikx} - e^{-ikx + 2ikl_1})(a_+ e^{-|k|y} + b_+ e^{-|k|y} + b_- e^{|k|y}),$$
$$0 < y < d_1 \tag{22}$$

$$\frac{1}{1 - e^{2ik(l_1 + l_2)}}(e^{ikx} - e^{-ikx + 2ikl_1})(a_- e^{|k|y} + b_- e^{|k|y} + b_+ e^{-|k|y}),$$
$$-d_2 < y < 0 \tag{23}$$

$$\frac{1}{1 - e^{2ik(l_1 + l_2)}}(e^{ikx} - e^{-ikx + 2ikl_1})(c_- e^{|k|y} + c_+ e^{-|k|y}),$$
$$-(d_2 + d_3) < y < -d_2 \tag{24}$$

where k is the wave vector of the transverse SP modes; a_- and a_+ are the expansion coefficients, which can be calculated by applying a Fourier transform to the dipole potential:

$$a_+ = \frac{p_y - ip_x \, \text{sgn}(k)}{2\varepsilon_0}, \quad a_- = \frac{-p_y - ip_x \, \text{sgn}(k)}{2\varepsilon_0} \tag{25}$$

The other four unknown coefficients b_-, b_+, c_-, and c_+ can be found through the boundary conditions at $y = \beta$ and $y = 2\pi - \theta + \beta$:

$$b_- = ((a_+ e^{2|k|(\theta - \beta) + \alpha}[e^{2|k|(2\pi - \theta)} - 1] + a_-(1 - e^{2|k|\pi})$$
$$+ a_- e^{2\alpha}[e^{2|k|\pi} - e^{2|k|(2\pi - \theta)}])/(e^{2\alpha}(e^{|k|(2\pi - \theta)} - e^{|k|\theta})^2$$
$$- (e^{2|k|\pi} - 1)^2)) \tag{26}$$

$$b_+ = ((a_- e^{2|k|\beta + \alpha}[e^{2|k|(2\pi - \theta)} - 1] + a_+(1 - e^{2|k|\pi})$$
$$+ a_+ e^{2\alpha}[e^{2|k|\pi} - e^{2|k|(2\pi - \theta)}])/(e^{2\alpha}(e^{|k|(2\pi - \theta)} - e^{|k|\theta})^2$$
$$- (e^{2|k|\pi} - 1)^2)) \tag{27}$$

$$c_- = \frac{2e^{2|k|\pi}}{\varepsilon_s + 1}((a_-(1 - e^{2|k|\pi}) + a_+ e^{\alpha}[e^{2|k|(\pi - \beta)} - e^{2|k|(\theta - \beta)}])$$
$$/(e^{2\alpha}(e^{|k|(2\pi - \theta)} - e^{|k|\theta})^2 - (e^{2|k|\pi} - 1)^2)) \tag{28}$$

$$c_+ = \frac{2}{\varepsilon_s + 1}((a_+(1 - e^{2|k|\pi}) + a_- e^{\alpha}[e^{2|k|(\pi - \theta + \beta)} - e^{2|k|\beta}])$$
$$/(e^{2\alpha}(e^{|k|(2\pi - \theta)} - e^{|k|\theta})^2 - (e^{2|k|\pi} - 1)^2)) \tag{29}$$

Substituting b_- and b_+ back into eqs 22 and 23, and applying an inverse Fourier transform to the induced potential leads to the solution in the real space:

$$\phi^{\text{sca}} = \frac{1}{2\varepsilon_0(l_1 + l_2)}\sum_n \left[p_y \left(\cos\frac{n\pi x}{l_1 + l_2} - \cos\frac{n\pi(x - 2l_1)}{l_1 + l_2} \right) \right.$$
$$\times (\Gamma_y e^{n\pi y/l_1 + l_2} + \Lambda_y e^{-n\pi y/l_1 + l_2}) + p_x \left(\sin\frac{n\pi x}{l_1 + l_2} + \sin\frac{n\pi(x - 2l_1)}{l_1 + l_2} \right)$$
$$\left. \times (\Gamma_x e^{n\pi y/l_1 + l_2} + \Lambda_x e^{-n\pi y/l_1 + l_2}) \right] \tag{30}$$

where

$$\Gamma_x = (e^{\alpha}(\gamma_3^{2n} - 1)\gamma_2^{2n} - e^{2\alpha}\gamma_3^{2n} + (e^{2\alpha} - 1)\gamma_1^n \gamma_2^n \gamma_3^n + 1)$$
$$/(e^{2\alpha}(\gamma_1^n \gamma_2^n - \gamma_3^n)^2 - (\gamma_1^n \gamma_2^n \gamma_3^n - 1)^2) \tag{31}$$

$$\Gamma_y = (e^{\alpha}(\gamma_3^{2n} - 1)\gamma_2^{2n} + e^{2\alpha}\gamma_3^{2n} - (e^{2\alpha} - 1)\gamma_1^n \gamma_2^n \gamma_3^n - 1)$$
$$/(e^{2\alpha}(\gamma_1^n \gamma_2^n - \gamma_3^n)^2 - (\gamma_1^n \gamma_2^n \gamma_3^n - 1)^2) \tag{32}$$

$$\Lambda_x = (e^{\alpha}(\gamma_3^{2n} - 1)\gamma_1^{2n} - e^{2\alpha}\gamma_3^{2n} + (e^{2\alpha} - 1)\gamma_1^n \gamma_2^n \gamma_3^n + 1)$$
$$/(e^{2\alpha}(\gamma_1^n \gamma_2^n - \gamma_3^n)^2 - (\gamma_1^n \gamma_2^n \gamma_3^n - 1)^2) \tag{33}$$

$$\Lambda_y = -((e^{\alpha}(\gamma_3^{2n} - 1)\gamma_1^{2n} + e^{2\alpha}\gamma_3^{2n} - (e^{2\alpha} - 1)\gamma_1^n \gamma_2^n \gamma_3^n - 1)$$
$$/(e^{2\alpha}(\gamma_1^n \gamma_2^n - \gamma_3^n)^2 - (\gamma_1^n \gamma_2^n \gamma_3^n - 1)^2)) \tag{34}$$

Here γ_1, γ_2, and γ_3 are constants defined after eq 13 in the former section. Equation 30 implies that, due to the finite size of the plasmonic cavity, the whole system only supports the SP modes with integer spatial frequencies. It is worth pointing out that, different from the singular nanostructures where the induced potential was calculated by considering only the propagating SP modes,[40−42,56,57,61] the calculation here takes into account the contribution from all the modes, including the lossy surface waves.[59]

The induced potential inside the metal slab can be obtained in a similar manner:

$$\phi^m = \frac{1}{\varepsilon_0(\varepsilon_m + 1)(l_1 + l_2)} \sum_n \left\{ p_y \left[\cos\frac{n\pi x}{l_1 + l_2} - \cos\frac{n\pi(x - 2l_1)}{l_1 + l_2} \right] \right.$$

$$\times (\Theta_y e^{n\pi y/l_1 + l_2} + \Omega_y e^{-n\pi y/l_1 + l_2}) + p_x \left[\sin\frac{n\pi x}{l_1 + l_2} + \sin\frac{n\pi(x - 2l_1)}{l_1 + l_2} \right]$$

$$\left. \times (\Theta_x e^{n\pi y/l_1 + l_2} + \Omega_x e^{-n\pi y/l_1 + l_2}) \right\} \quad (35)$$

where

$$\Theta_x = \frac{e^\alpha \gamma_2^n(\gamma_1^{-n}\gamma_3^n - \gamma_2^n) - \gamma_1^n\gamma_2^n\gamma_3^n + 1}{e^{2\alpha}(\gamma_1^n\gamma_2^n - \gamma_3^n)^2 - (\gamma_1^n\gamma_2^n\gamma_3^n - 1)^2} \quad (36)$$

$$\Theta_y = \frac{e^\alpha \gamma_2^n(\gamma_1^{-n}\gamma_3^n - \gamma_2^n) + \gamma_1^n\gamma_2^n\gamma_3^n - 1}{e^{2\alpha}(\gamma_1^n\gamma_2^n - \gamma_3^n)^2 - (\gamma_1^n\gamma_2^n\gamma_3^n - 1)^2} \quad (37)$$

$$\Omega_x = \frac{e^\alpha \gamma_1^{2n}\gamma_3^n(\gamma_3^n - \gamma_1^n\gamma_2^n) - \gamma_1^n\gamma_2^n\gamma_3^n(\gamma_1^n\gamma_2^n\gamma_3^n - 1)}{e^{2\alpha}(\gamma_1^n\gamma_2^n - \gamma_3^n)^2 - (\gamma_1^n\gamma_2^n\gamma_3^n - 1)^2} \quad (38)$$

$$\Omega_y = \frac{e^\alpha \gamma_1^{2n}\gamma_3^n(\gamma_1^n\gamma_2^n - \gamma_3^n) - \gamma_1^n\gamma_2^n\gamma_3^n(\gamma_1^n\gamma_2^n\gamma_3^n - 1)}{e^{2\alpha}(\gamma_1^n\gamma_2^n - \gamma_3^n)^2 - (\gamma_1^n\gamma_2^n\gamma_3^n - 1)^2} \quad (39)$$

The electric fields in each region can then be derived by differentiating the potential:

$$E_x^{sca} = \sum_n \frac{n\pi}{2\varepsilon_0(l_1+l_2)^2} \left[p_y \left(\sin\frac{n\pi x}{l_1 + l_2} - \sin\frac{n\pi(x - 2l_1)}{l_1 + l_2} \right) \right.$$

$$\times (\Gamma_y e^{n\pi y/l_1 + l_2} + \Lambda_y e^{-n\pi y/l_1 + l_2}) - p_x \left(\cos\frac{n\pi x}{l_1 + l_2} + \cos\frac{n\pi(x - 2l_1)}{l_1 + l_2} \right)$$

$$\left. \times (\Gamma_x e^{n\pi y/l_1 + l_2} + \Lambda_x e^{-n\pi y/l_1 + l_2}) \right] \quad (40)$$

$$E_y^{sca} = -\sum_n \frac{n\pi}{2\varepsilon_0(l_1+l_2)^2} \left[p_y \left(\cos\frac{n\pi x}{l_1 + l_2} - \cos\frac{n\pi(x - 2l_1)}{l_1 + l_2} \right)(\Gamma_y e^{n\pi y/l_1 + l_2} \right.$$

$$- \Lambda_y e^{-n\pi y/l_1 + l_2}) + p_x \left(\sin\frac{n\pi x}{l_1 + l_2} + \sin\frac{n\pi(x - 2l_1)}{l_1 + l_2} \right)$$

$$\left. \times (\Gamma_x e^{n\pi y/l_1 + l_2} - \Lambda_x e^{-n\pi y/l_1 + l_2}) \right] \quad (41)$$

$$E_x^m = \sum_n \frac{n\pi}{\varepsilon_0(\varepsilon_s + 1)(l_1+l_2)^2} \left\{ p_y \left[\sin\frac{n\pi x}{l_1 + l_2} - \sin\frac{n\pi(x - 2l_1)}{l_1 + l_2} \right] \right.$$

$$(\Gamma_y e^{n\pi y/l_1 + l_2} + \Lambda_y e^{-n\pi y/l_1 + l_2}) - p_x \left[\cos\frac{n\pi x}{l_1 + l_2} + \cos\frac{n\pi(x - 2l_1)}{l_1 + l_2} \right]$$

$$\left. \times (\Gamma_x e^{n\pi y/l_1 + l_2} + \Lambda_x e^{-n\pi y/l_1 + l_2}) \right\} \quad (42)$$

$$E_y^m = -\sum_n \frac{n\pi}{\varepsilon_0(\varepsilon_s + 1)(l_1+l_2)^2} \left\{ p_y \left[\cos\frac{n\pi x}{l_1 + l_2} - \cos\frac{n\pi(x - 2l_1)}{l_1 + l_2} \right] \right.$$

$$\times (\Gamma_y e^{n\pi y/l_1 + l_2} - \Lambda_y e^{-n\pi y/l_1 + l_2}) + p_x \left[\sin\frac{n\pi x}{l_1 + l_2} + \sin\frac{n\pi(x - 2l_1)}{l_1 + l_2} \right]$$

$$\left. \times (\Gamma_x e^{n\pi y/l_1 + l_2} - \Lambda_x e^{-n\pi y/l_1 + l_2}) \right\} \quad (43)$$

Extinction Cross-Section. Now we can compute the power dissipated by each dipole in the original slab geometry. From

the expression of the scattered field eqs 40 and 41, we can directly obtain the electric field at the dipole position:

$$E_x^{sca}(z = 0) = \sum_n \frac{n\pi}{2\varepsilon_0(l_1+l_2)^2} \left[p_y \left(\sin\frac{2n\pi l_1}{l_1 + l_2} \right)(\Gamma_y + \Lambda_y) \right.$$

$$\left. - p_x \left(1 + \cos\frac{2n\pi l_1}{l_1 + l_2} \right)(\Gamma_x + \Lambda_x) \right] \quad (44)$$

$$E_y^{sca}(z = 0) = -\sum_n \frac{n\pi}{2\varepsilon_0(l_1+l_2)^2} \left[p_y \left(1 - \cos\frac{2n\pi l_1}{l_1 + l_2} \right) \right.$$

$$\left. \times (\Gamma_y - \Lambda_y) + p_x \left(\sin\frac{2n\pi l_1}{l_1 + l_2} \right)(\Gamma_x - \Lambda_x) \right] \quad (45)$$

Then the dissipated power can be deduced from this back-scattered field:

$$P_a = -\frac{\omega}{2} \text{Im}\{\bar{p}^* \cdot \bar{E}^{sca}(z = 0)\}$$

$$= -\frac{\omega}{2\varepsilon_0(l_1+l_2)^2} (\text{Im}\{\xi_{xx}\}|p_x|^2 + \text{Im}\{\xi_{yy}\}|p_y|^2) \quad (46)$$

where ω is the angular frequency; $\bar{p}^*$ denotes the complex conjugate of the dipole moment $\bar{p}$; ξ_{xx} and ξ_{yy} are defined by eqs 11 and 12. As energy is conserved under the transformation, eq 46 also accounts for the power absorbed by the nanowire pair in the transformed x'-y' coordinate frame. Thus, normalizing P_a by the incident power flux $P_0' = c_0\varepsilon_0|\bar{E}_0'|^2/2$ (where c_0 is the speed of light in free space), we can derive the extinction cross-section of the nanowire pair in the quasi-static approximation:

$$\sigma_e^x = \frac{P_a^x}{P_0'} = -\frac{4\pi^2\omega a^2}{c_0(l_1+l_2)^2} \text{Im}\{\xi_{xx}\},$$

$$\sigma_e^y = \frac{P_a^y}{P_0'} = -\frac{4\pi^2\omega a^2}{c_0(l_1+l_2)^2} \text{Im}\{\xi_{yy}\} \quad (47)$$

Injecting $\omega = c_0 k_0$, $l_1 = \pi\tau_1$, and $l_2 = \pi\tau_2$, eq 47 is reduced to eq 9. *Scattering Cross-Section.* The net dipole moment of the nanowire dimer can be deduced from the total electric field at the origin of the slab geometry (x–y frame):

$$\bar{p}^{dim} = 2\pi\varepsilon_0 a \times \bar{E}^{tot*}(z = 0) \quad (48)$$

This in turns gives the scattered field in the transformed frame:

$$\bar{E}'^{sca}(z' \to \infty) = -\frac{ik_0^2}{8\varepsilon_0}\bar{p}^{dim} = -\frac{i\pi k_0^2 a}{4} \times \bar{E}^{tot*}(z = 0) \quad (49)$$

As pointed out in previous studies,[43,46] this uniform scattered field can be related to an array of absorbing particles in the original coordinate (x–y frame). Each particle has a dipole moment:

$$\bar{p}^{abs} = 2\pi\varepsilon_0 a \times \bar{E}'^{sca*}(z' \to \infty) \quad (50)$$

Substituting eq 49 into eq 50 yields:

$$\bar{p}^{abs} = -\frac{i\varepsilon_0\pi^2 k_0^2 a^2}{2} \times \bar{E}^{tot}(z = 0) \quad (51)$$

Under the quasi-static approximation, the total electric field is approximately equal to the scattered field in the slab geometry ($\bar{E}^{tot} \approx \bar{E}^{sca}$). Hence, the power dissipated by the absorbing particle is calculated as

$$P_s = \frac{\omega}{2} \text{Im}\{\bar{p}^{abs*} \cdot \bar{E}^{tot}(z = 0)\}$$

$$\approx \frac{\omega\varepsilon_0\pi^2 k_0^2 a^2}{4} (|E_x^{sca}(z = 0)|^2 + |E_y^{sca}(z = 0)|^2) \quad (52)$$

Substituting eqs 44 and 45 into the above equation, and renormalizing P_s by the incident power flux P_0', the scattering cross-section of the nanowire dimer can be obtained (see eq 10).

Radiative Damping. When the total dimension of the nanowire pair is larger than 20 nm, the total electric field $\bar{E}^{tot}$ is no longer equal to $\bar{E}^{sca}$. In this case, we have to recalculate $\bar{E}^{tot}$ using the net dipole moment $\bar{p} + \bar{p}^{abs}$ in the original slab geometry. Detailed algebraic operations show that the total electric field at the dipole position takes the following form:

$$E_x^{tot}(z=0) = -\frac{1}{\varepsilon_0(l_1+l_2)^2}[\xi_{xx}(p_x+p_x^{abs}) + \xi_{xy}(p_y+p_y^{abs})] \quad (53)$$

$$E_y^{tot}(z=0) = -\frac{1}{\varepsilon_0(l_1+l_2)^2}[\xi_{yy}(p_y+p_y^{abs}) - \xi_{xy}(p_x+p_x^{abs})] \quad (54)$$

By substituting eq 51 into eqs 53 and 54, we can derive the total electric field the dipole position:

$$E_x^{tot}(z=0) = -\frac{1}{\varepsilon_0(l_1+l_2)^2}\frac{[\xi_{xx}+i\eta(\xi_{xx}\xi_{yy}+\xi_{xy}^2)]p_x + \xi_{xy}p_y}{(1+i\eta\xi_{xx})(1+i\eta\xi_{yy}) - (\eta\xi_{xy})^2} \quad (55)$$

$$E_y^{tot}(z=0) = -\frac{1}{\varepsilon_0(l_1+l_2)^2}\frac{[\xi_{yy}+i\eta(\xi_{xx}\xi_{yy}+\xi_{xy}^2)]p_y - \xi_{xy}p_x}{(1+i\eta\xi_{xx})(1+i\eta\xi_{yy}) - (\eta\xi_{xy})^2} \quad (56)$$

where η is a constant defined by eq 17. Then the power dissipated by the emitting dipole can be deduced:

$$P_a = \frac{\omega}{2}\text{Im}\{\bar{p}^*\cdot\bar{E}^{tot}(z=0)\} = -\frac{\omega}{2\varepsilon_0(l_1+l_2)^2}$$

$$\times\text{Im}\left\{\frac{[\xi_{xx}+i\eta(\xi_{xx}\xi_{yy}+\xi_{xy}^2)]p_x^2 + [\xi_{yy}+i\eta(\xi_{xx}\xi_{yy}+\xi_{xy}^2)]p_y^2}{(1+i\eta\xi_{xx})(1+i\eta\xi_{yy}) - (i\eta\xi_{xy})^2}\right\} \quad (57)$$

Normalizing the above equation by P_0' gives the modified extinction cross-section characterized by eq 15.

The modified scattering cross-section of the nanowire dimer is related to the power dissipated by the fictional absorbing dipole:

$$P_s = \frac{\omega}{2}\text{Im}\{\bar{p}^{abs*}\cdot\bar{E}^{tot}(z=0)\}$$

$$= \frac{\omega\pi^2k_0^2a^2}{4\varepsilon_0(l_1+l_2)^2}\left\{\left|\frac{[\xi_{xx}+iD(\xi_{xx}\xi_{yy}+\xi_{xy}^2)]p_x + \xi_{xy}p_y}{(1+iD\xi_{xx})(1+iD\xi_{yy}) - (D\xi_{xy})^2}\right|^2\right.$$

$$\left.+ \left|\frac{[\xi_{yy}+iD(\xi_{xx}\xi_{yy}+\xi_{xy}^2)]p_y - \xi_{xy}p_x}{(1+iD\xi_{xx})(1+iD\xi_{yy}) - (D\xi_{xy})^2}\right|^2\right\} \quad (58)$$

Renormalizing P_s by P_0' leads to eq 16.

Crescent-Shaped Cylinder. The 2D nanocrescent with symmetric blunt tips has already been investigated in ref 43. Following the same procedure, the extinction and scattering cross sections of the asymmetric crescent structure can be obtained:

$$\sigma_e^x = -4k_0\left(\frac{D\sin\beta}{\tau_1+\tau_2}\right)^2\text{Im}\left\{\frac{\xi_{xx}+i\eta(\xi_{xx}\xi_{yy}+\xi_{xy}^2)}{(1+i\eta\xi_{xx})(1+i\eta\xi_{yy}) - (\eta\xi_{xy})^2}\right\}$$

$$\sigma_e^y = -4k_0\left(\frac{D\sin\beta}{\tau_1+\tau_2}\right)^2\text{Im}\left\{\frac{\xi_{yy}+i\eta(\xi_{xx}\xi_{yy}+\xi_{xy}^2)}{(1+i\eta\xi_{xx})(1+i\eta\xi_{yy}) - (\eta\xi_{xy})^2}\right\} \quad (59)$$

$$\sigma_s^x = 2k_0^3\left(\frac{D\sin\beta}{\tau_1+\tau_2}\right)^4\left(\left|\frac{\xi_{xx}+i\eta(\xi_{xx}\xi_{yy}+\xi_{xy}^2)}{(1+i\eta\xi_{xx})(1+i\eta\xi_{yy}) - (\eta\xi_{xy})^2}\right|^2\right.$$

$$\left.+ \left|\frac{\xi_{xy}}{(1+i\eta\xi_{xx})(1+i\eta\xi_{yy}) - (\eta\xi_{xy})^2}\right|^2\right)$$

$$\sigma_s^y = 2k_0^3\left(\frac{D\sin\beta}{\tau_1+\tau_2}\right)^4\left[\left|\frac{\xi_{yy}+i\eta(\xi_{xx}\xi_{yy}+\xi_{xy}^2)}{(1+i\eta\xi_{xx})(1+i\eta\xi_{yy}) - (\eta\xi_{xy})^2}\right|^2\right.$$

$$\left.+ \left|\frac{\xi_{xy}}{(1+i\eta\xi_{xx})(1+i\eta\xi_{yy}) - (\eta\xi_{xy})^2}\right|^2\right] \quad (60)$$

Here $\tau_{1(2)} = l_{1(2)}/\pi$; the coefficients ξ_{xx}, ξ_{yy}, ξ_{xy}, and η take the following form:

$$\xi_{xx} = \sum_n \frac{n\pi}{2}\left(1 - \cos\frac{2n\pi\tau_1}{\tau_1+\tau_2}\right)$$

$$\times\frac{e^\alpha(\gamma_3^{2n}-1)(\gamma_1^{2n}+\gamma_2^{2n}) - 2e^{2\alpha}\gamma_3^{2n} + 2(e^{2\alpha}-1)\gamma_1^n\gamma_2^n\gamma_3^n + 2}{e^{2\alpha}(\gamma_1^n\gamma_2^n - \gamma_3^n)^2 - (\gamma_1^n\gamma_2^n\gamma_3^n - 1)^2} \quad (61)$$

$$\xi_{yy} = \sum_n \frac{n\pi}{2}\left(1 + \cos\frac{2n\pi\tau_1}{\tau_1+\tau_2}\right)$$

$$\times\frac{e^\alpha(\gamma_3^{2n}-1)(\gamma_1^{2n}+\gamma_2^{2n}) + 2e^{2\alpha}\gamma_3^{2n} - 2(e^{2\alpha}-1)\gamma_1^n\gamma_2^n\gamma_3^n - 2}{e^{2\alpha}(\gamma_1^n\gamma_2^n - \gamma_3^n)^2 - (\gamma_1^n\gamma_2^n\gamma_3^n - 1)^2} \quad (62)$$

$$\xi_{xy} = \left(\frac{\varepsilon_m - 1}{\varepsilon_m + 1}\right)\sum_n \frac{n\pi}{2}\left(\sin\frac{2n\pi\tau_1}{\tau_1+\tau_2}\right)$$

$$\times\frac{(e^{2n\pi d_3/L} - 1)(\gamma_2^n + \gamma_1^n)(\gamma_2^n - \gamma_1^n)}{e^{2\alpha}(\gamma_1^n\gamma_2^n - \gamma_3^n)^2 - (\gamma_1^n\gamma_2^n\gamma_3^n - 1)^2} \quad (63)$$

$$\eta = \frac{1}{2}\left(\frac{k_0D\sin\beta}{\tau_1+\tau_2}\right)^2 \quad (64)$$

where

$$\gamma_1 = e^{\beta/(\tau_1+\tau_2)}, \gamma_2 = e^{(2\pi-\theta-\beta)/(\tau_1+\tau_2)}, \gamma_3 = e^{\theta/(\tau_1+\tau_2)}$$

Conflict of Interest: The authors declare no competing financial interest.

REFERENCES AND NOTES

1. Kuhn, S.; Hakanson, U.; Rogobete, L.; Sandoghdar, V. Enhancement of Single-Molecule Fluorescence Using a Gold Nanoparticle as an Optical Nanoantenna. *Phys. Rev. Lett.* **2006**, *97*, 017402.
2. Bouhelier, A.; Bachelot, R.; Lerondel, G.; Kostcheev, S.; Royer, P.; Wiederrecht, G. P. Surface Plasmon Characteristics of Tunable Photoluminescence in Single Gold Nanorods. *Phys. Rev. Lett.* **2005**, *95*, 267405.
3. Pendry, J. B. Negative Refraction Makes a Perfect Lens. *Phys. Rev. Lett.* **2000**, *85*, 3966–3969.
4. Fang, N.; Lee, H.; Sun, C.; Zhang, X. Sub-Diffraction-Limited Optical Imaging with a Silver Superlens. *Science* **2005**, *308*, 534–537.
5. Moskovits, M. Surface-Enhanced Spectroscopy. *Rev. Mod. Phys.* **1985**, *57*, 783–826.
6. Nie, S. M.; Emery, S. R. Probing Single Molecules and Single Nanoparticles by Surface-Enhanced Raman Scattering. *Science* **1997**, *275*, 1102–1106.
7. Kneipp, K.; Wang, Y.; Kneipp, H.; Perelman, L. T.; Itzkan, I.; Dasari, R.; Feld, M. S. Single Molecule Detection Using Surface-Enhanced Raman Scattering (SERS). *Phys. Rev. Lett.* **1997**, *78*, 1667–1670.
8. Kim, S.; Jin, J. H.; Kim, Y. J.; Park, I. Y.; Kim, Y.; Kim, S. W. High-Harmonic Generation by Resonant Plasmon Field Enhancement. *Nature* **2008**, *453*, 757–760.
9. Zhang, Y.; Grady, N. K.; Ayala-Orozco, C.; Halas, N. J. Three-Dimensional Nanostructures as Highly Efficient Generators of Second Harmonic Light. *Nano Lett.* **2011**, *11*, 5519–5523.
10. Navarro-Cia, M.; Maier, S. A. Broad-Band Near-Infrared Plasmonic Nanoantennas for Higher Harmonic Generation. *ACS Nano* **2012**, *6*, 3537–3544.

11. Barnes, W. L.; Dereux, A.; Ebbesen, T. W. Surface Plasmon Subwavelength Optics. *Nature* **2003**, *424*, 824–830.
12. Gramotnev, D. K.; Bozhevolnyi, S. I. Plasmonics beyond the Diffraction Limit. *Nat. Photonics* **2010**, *4*, 83–91.
13. Halas, N. J. Plasmonics: An Emerging Field Fostered by Nano Letters. *Nano Lett.* **2010**, *10*, 3816–3822.
14. Halas, N. J.; Lal, S.; Chang, W. S.; Link, S.; Nordlander, P. Plasmons in Strongly Coupled Metallic Nanostructures. *Chem. Rev.* **2011**, *111*, 3913–3961.
15. Rycenga, M.; Cobley, C. M.; Zeng, J.; Li, W. Y.; Moran, C. H.; Zhang, Q.; Qin, D.; Xia, Y. N. Controlling the Synthesis and Assembly of Silver Nanostructures for Plasmonic Applications. *Chem. Rev.* **2011**, *111*, 3669–3712.
16. Giannini, V.; Fernandez-Dominguez, A. I.; Heck, S. C.; Maier, S. A. Plasmonic Nanoantennas: Fundamentals and Their Use in Controlling the Radiative Properties of Nanoemitters. *Chem. Rev.* **2011**, *111*, 3888–3912.
17. Maier, S. A.; Atwater, H. A. Plasmonics: Localization and Guiding of Electromagnetic Energy in Metal/Dielectric Structures. *J. Appl. Phys.* **2005**, *98*, 011101.
18. GarciaVidal, F. J.; Pendry, J. B. Collective Theory for Surface Enhanced Raman Scattering. *Phys. Rev. Lett.* **1996**, *77*, 1163–1166.
19. Pendry, J. B.; Martin-Moreno, L.; Garcia-Vidal, F. J. Mimicking Surface Plasmons with Structured Surfaces. *Science* **2004**, *305*, 847–848.
20. Moreno, E.; Rodrigo, S. G.; Bozhevolnyi, S. I.; Martin-Moreno, L.; Garcia-Vidal, F. J. Guiding and Focusing of Electromagnetic Fields with Wedge Plasmon Polaritons. *Phys. Rev. Lett.* **2008**, *100*, 023901.
21. Martin-Cano, D.; Martin-Moreno, L.; Garcia-Vidal, F. J.; Moreno, E. Resonance Energy Transfer and Superradiance Mediated by Plasmonic Nanowaveguides. *Nano Lett.* **2010**, *10*, 3129–3134.
22. Stockman, M. I. Nanofocusing of Optical Energy in Tapered Plasmonic Waveguides. *Phys. Rev. Lett.* **2004**, *93*, 137404.
23. Bozhevolnyi, S. I.; Volkov, V. S.; Devaux, E.; Laluet, J. Y.; Ebbesen, T. W. Channel Plasmon Subwavelength Waveguide Components Including Interferometers and Ring Resonators. *Nature* **2006**, *440*, 508–511.
24. Oulton, R. F.; Sorger, V. J.; Zentgraf, T.; Ma, R. M.; Gladden, C.; Dai, L.; Bartal, G.; Zhang, X. Plasmon Lasers at Deep Subwavelength Scale. *Nature* **2009**, *461*, 629–632.
25. Zhang, J. J.; Xiao, S. S.; Wubs, M.; Mortensen, N. A. Surface Plasmon Wave Adapter Designed with Transformation Optics. *ACS Nano* **2011**, *5*, 4359–4364.
26. Hill, R. T.; Mock, J. J.; Urzhumov, Y.; Sebba, D. S.; Oldenburg, S. J.; Chen, S. Y.; Lazarides, A. A.; Chilkoti, A.; Smith, D. R. Leveraging Nanoscale Plasmonic Modes to Achieve Reproducible Enhancement of Light. *Nano Lett.* **2010**, *10*, 4150–4154.
27. Atay, T.; Song, J. H.; Nurmikko, A. V. Strongly Interacting Plasmon Nanoparticle Pairs: From Dipole–Dipole Interaction to Conductively Coupled Regime. *Nano Lett.* **2004**, *4*, 1627–1631.
28. Lassiter, J. B.; Aizpurua, J.; Hernandez, L. I.; Brandl, D. W.; Romero, I.; Lal, S.; Hafner, J. H.; Nordlander, P.; Halas, N. J. Close Encounters between Two Nanoshells. *Nano Lett.* **2008**, *8*, 1212–1218.
29. Brown, L. V.; Sobhani, H.; Lassiter, J. B.; Nordlander, P.; Halas, N. J. Heterodimers: Plasmonic Properties of Mismatched Nanoparticle Pairs. *ACS Nano* **2010**, *4*, 819–832.
30. Rochholz, H.; Bocchio, N.; Kreiter, M. Tuning Resonances on Crescent-Shaped Noble-Metal Nanoparticles. *New J. Phys.* **2007**, *9*, 53.
31. Bukasov, R.; Shumaker-Parry, J. S. Highly Tunable Infrared Extinction Properties of Gold Nanocrescents. *Nano Lett.* **2007**, *7*, 1113–1118.
32. Bukasov, R.; Ali, T. A.; Nordlander, P.; Shumaker-Parry, J. S. Probing the Plasmonic Near-Field of Gold Nanocrescent Antennas. *ACS Nano* **2010**, *4*, 6639–6650.
33. Mirin, N. A.; Ali, T. A.; Nordlander, P.; Halas, N. J. Perforated Semishells: Far-Field Directional Control and Optical Frequency Magnetic Response. *ACS Nano* **2010**, *4*, 2701–2712.
34. Lei, D. Y.; Fernandez-Dominguez, A. I.; Sonnefraud, Y.; Appavoo, K.; Haglund, R. F.; Pendry, J. B.; Maier, S. A. Revealing Plasmonic Gap Modes in Particle-on-Film Systems Using Dark-Field Spectroscopy. *ACS Nano* **2012**, *6*, 3537–3544.
35. Ward, A. J.; Pendry, J. B. Refraction and Geometry in Maxwell's Equations. *J. Mod. Opt* **1996**, *43*, 773–793.
36. Pendry, J. B.; Schurig, D.; Smith, D. R. Controlling Electromagnetic Fields. *Science* **2006**, *312*, 1780–1782.
37. Mcphedran, R. C.; Mckenzie, D. R. Electrostatic and Optical Resonances of Arrays of Cylinders. *Appl. Phys.* **1980**, *23*, 223–235.
38. Mcphedran, R. C.; Perrins, W. T. Electrostatic and Optical Resonances of Cylinder Pairs. *Appl. Phys.* **1981**, *24*, 311–318.
39. Mcphedran, R. C.; Milton, G. W. Transport-Properties of Touching Cylinder Pairs and of the Square Array of Touching Cylinders. *Proc. R. Soc. A* **1987**, *411*, 313–326.
40. Aubry, A.; Lei, D. Y.; Fernandez-Dominguez, A. I.; Sonnefraud, Y.; Maier, S. A.; Pendry, J. B. Plasmonic Light-Harvesting Devices over the Whole Visible Spectrum. *Nano Lett.* **2010**, *10*, 2574–2579.
41. Luo, Y.; Pendry, J. B.; Aubry, A. Surface Plasmons and Singularities. *Nano Lett.* **2010**, *10*, 4186–4191.
42. Fernandez-Dominguez, A. I.; Maier, S. A.; Pendry, J. B. Collection and Concentration of Light by Touching Spheres: A Transformation Optics Approach. *Phys. Rev. Lett.* **2010**, *105*, 266807.
43. Luo, Y.; Lei, D. Y.; Maier, S. A.; Pendry, J. B. Broadband Light Harvesting Nanostructures Robust to Edge Bluntness. *Phys. Rev. Lett.* **2012**, *108*, 023901.
44. Zuloaga, J.; Prodan, E.; Nordlander, P. Quantum Description of the Plasmon Resonances of a Nanoparticle Dimer. *Nano Lett.* **2009**, *9*, 887–891.
45. Zuloaga, J.; Prodan, E.; Nordlander, P. Quantum Plasmonics: Optical Properties and Tunability of Metallic Nanorods. *ACS Nano* **2010**, *4*, 5269–5276.
46. Aubry, A.; Lei, D. Y.; Maier, S. A.; Pendry, J. B. Interaction between Plasmonic Nanoparticles Revisited with Transformation Optics. *Phys. Rev. Lett.* **2010**, *105*, 233901.
47. Aubry, A.; Lei, D. Y.; Maier, S. A.; Pendry, J. B. Plasmonic Hybridization between Nanowires and a Metallic Surface: A Transformation Optics Approach. *ACS Nano* **2011**, *5*, 3293–3308.
48. Luk'yanchuk, B.; Zheludev, N. I.; Maier, S. A.; Halas, N. J.; Nordlander, P.; Giessen, H.; Chong, C. T. The Fano Resonance in Plasmonic Nanostructures and Metamaterials. *Nat. Mater.* **2010**, *9*, 707–715.
49. Hao, F.; Sonnefraud, Y.; Van Dorpe, P.; Maier, S. A.; Halas, N. J.; Nordlander, P. Symmetry Breaking in Plasmonic Nanocavities: Subradiant LSPR Sensing and a Tunable Fano Resonance. *Nano Lett.* **2008**, *8*, 3983–3988.
50. Verellen, N.; Sonnefraud, Y.; Sobhani, H.; Hao, F.; Moshchalkov, V. V.; Van Dorpe, P.; Nordlander, P.; Maier, S. A. Fano Resonances in Individual Coherent Plasmonic Nanocavities. *Nano Lett.* **2009**, *9*, 1663–1667.
51. Zhang, S.; Genov, D. A.; Wang, Y.; Liu, M.; Zhang, X. Plasmon-Induced Transparency in Metamaterials. *Phys. Rev. Lett.* **2008**, *101*, 047401.
52. Liu, N.; Langguth, L.; Weiss, T.; Kastel, J.; Fleischhauer, M.; Pfau, T.; Giessen, H. Plasmonic Analogue of Electromagnetically Induced Transparency at the Drude Damping Limit. *Nat. Mater.* **2009**, *8*, 758–762.
53. Hao, F.; Nordlander, P.; Sonnefraud, Y.; Van Dorpe, P.; Maier, S. A. Tunability of Subradiant Dipolar and Fano-Type Plasmon Resonances in Metallic Ring/Disk Cavities: Implications for Nanoscale Optical Sensing. *ACS Nano* **2009**, *3*, 643–652.
54. Fang, Z. Y.; Cai, J. Y.; Yan, Z. B.; Nordlander, P.; Halas, N. J.; Zhu, X. Removing a Wedge from a Metallic Nanodisk Reveals a Fano Resonance. *Nano Lett.* **2011**, *11*, 4475–4479.
55. Rahmani, M.; Lei, D. Y.; Giannini, V.; Lukiyanchuk, B.; Ranjbar, M.; Liew, T. Y. F.; Hong, M. H.; Maier, S. A. Subgroup Decomposition of Plasmonic Resonances in Hybrid Oligomers: Modeling the Resonance Lineshape. *Nano Lett.* **2012**, *12*, 3308–3314.

56. Lei, D. Y.; Aubry, A.; Luo, Y.; Maier, S. A.; Pendry, J. B. Plasmonic Interaction between Overlapping Nanowires. *ACS Nano* **2011**, *5*, 597–607.

57. Luo, Y.; Aubry, A.; Pendry, J. B. Electromagnetic Contribution to Surface-Enhanced Raman Scattering from Rough Metal Surfaces: A Transformation Optics Approach. *Phys. Rev. B* **2011**, *83*, 155422.

58. Jackson, J. D. *Classical Electrodynamics*, 2nd ed.; Wiley: New York, 1975.

59. Aubry, A.; Lei, D. Y.; Maier, S. A.; Pendry, J. B. Conformal Transformation Applied to Plasmonics beyond the Quasi-static Limit. *Phys. Rev. B* **2010**, *82*, 205109.

60. Palik, E. D. *Handbook of Optical Constants of Solids II*; Academic Press: Boston, 1991.

61. Lei, D. Y.; Aubry, A.; Maier, S. A.; Pendry, J. B. Broadband Nano-focusing of Light Using Kissing Nanowires. *New J. Phys.* **2010**, *12*, 093030.

62. Prodan, E.; Radloff, C.; Halas, N. J.; Nordlander, P. A Hybridization Model for the Plasmon Response of Complex Nanostructures. *Science* **2003**, *302*, 419–422.

63. Nordlander, P.; Prodan, E. Plasmon Hybridization in Nanoparticles near Metallic Surfaces. *Nano Lett.* **2004**, *4*, 2209–2213.

64. Steele, J. M.; Grady, N. K.; Nordlander, P.; Halas, N. J. Plasmon Hybridization in Complex Nanostructures. *Springer Ser. Opt. Sci.* **2007**, *131*, 183–196.

65. Willingham, B.; Brandl, D. W.; Nordlander, P. Plasmon Hybridization in Nanorod Dimers. *Appl. Phys. B* **2008**, *93*, 209–216.

66. Marinica, D. C.; Kazansky, A. K.; Nordlander, P.; Aizpurua, J.; Borisov, A. G. Quantum Plasmonics: Nonlinear Effects in the Field Enhancement of a Plasmonic Nanoparticle Dimer. *Nano Lett.* **2012**, *12*, 1333–1339.

67. Esteban, R.; Borisov, A. G.; Nordlander, P.; Aizpurua, J. Bridging Quantum and Classical Plasmonics with a Quantum-Corrected Model. *Nat. Commun.* **2012**, *3*, 825.

68. McMahon, J. M.; Gray, S. K.; Schatz, G. C. Optical Properties of Nanowire Dimers with a Spatially Nonlocal Dielectric Function. *Nano Lett.* **2010**, *10*, 3473–3481.

69. Fernandez-Dominguez, A. I.; Wiener, A.; Garcia-Vidal, F. J.; Maier, S. A.; Pendry, J. B. Transformation-Optics Description of Nonlocal Effects in Plasmonic Nanostructures. *Phys. Rev. Lett.* **2012**, *108*, 023901.